

Substitutional and surface Mn^{2+} centers in cubic ZnS:Mn nanocrystals. A correlated EPR and photoluminescence study

M. Stefan,¹ S. V. Nistor,¹ D. Ghica,¹ C. D. Mateescu,¹ M. Nikl,² and R. Kucerkova²

¹National Institute of Materials Physics, POB MG-7, RO-077125 Magurele, Romania

²Institute of Physics, Academy of Sciences of the Czech Republic, Cukrovarnicka 10, CZ-16253 Prague, Czech Republic

(Received 27 May 2010; revised manuscript received 7 October 2010; published 20 January 2011)

The EPR, radioluminescence, and photoluminescence of cubic ZnS (cZnS) nanocrystals (NCs) with a narrow size distribution centered at 2 nm, doped with 0.1, 0.2, and 0.5 at. % Mn^{2+} ions were investigated. Besides the main lines from substitutional Mn^{2+} ions localized in the core of the NCs next to a stacking defect, the EPR spectra exhibited two broader hyperfine sextets, attributed to the so-called Mn(II) and Mn(III) surface centers, which could be separated by adequate thermal treatments. The contribution to the photoluminescence from the Mn^{2+} ions at various sites was further determined from the analysis of the steady-state and time-resolved photoluminescence data from cZnS:Mn NCs subjected to thermal treatments and from cZnS:Mn single crystals. Thus, the main emission consisting of two intense overlapping bands peaking at 596 and 630 nm was attributed to the ${}^4T_1-{}^6A_1$ transition of the substitutional Mn^{2+} ions in the core of the cZnS nanocrystals and to residual aggregated Mn^{2+} ions, respectively, the last ones being responsible for a broad EPR line observed in the X -band spectrum. The Mn(II) and Mn(III) centers, consisting of Mn^{2+} ions in the oxidized and hydrolyzed surface layer of the NCs, respectively, are only indirectly involved in the energy transfer to the substitutional Mn^{2+} centers, very likely through pairs interaction.

DOI: [10.1103/PhysRevB.83.045301](https://doi.org/10.1103/PhysRevB.83.045301)

PACS number(s): 76.30.Fc, 78.55.Et, 78.67.Bf

I. INTRODUCTION

The synthesis and study of nanostructured wide band-gap semiconductors doped with impurity ions has been a major area of interdisciplinary research for the past two decades owing to expected spectacular changes in their physical properties as the size of the particles approaches the exciton Bohr radius.¹ In the case of the cubic ZnS nanocrystals (NCs) doped with Mn^{2+} ions (cZnS:Mn), a dramatic increase in both quantum luminescence efficiency and lifetime shortening was initially reported and attributed to quantum confinement (QC).² Later experiments evidenced essentially no change in the Mn^{2+} emission lifetime.^{3,4} The observed effects were attributed to other factors, such as the localization of a large fraction of the impurity ions near the surface of the nanocrystals, where they experience a different crystal field, an effect which could be further influenced by the capping compounds added to stabilize the NCs and/or to further improve the desired optical properties.^{5,6} Other possible factors included the clustering of impurities and the presence of neighboring lattice defects, in particular, vacancies, with resulting changes in the local crystal field at the impurity ions.^{3,4}

Electron paramagnetic resonance (EPR) spectroscopy can distinguish with high sensitivity the presence of paramagnetic ions at different lattice sites, determine changes in the local crystal-field symmetry, and provide information concerning the properties of the ground electronic state.⁷ Such information is contained in the spin Hamiltonian (SH), which describes the properties of the EPR spectra. In the case of NCs doped with paramagnetic ions the determination of the SH parameters is a difficult task, as many features related with the anisotropy of the EPR properties are hidden in the experimental spectrum, which is a superposition of averaged spectra from paramagnetic ions in NCs with various orientations in the magnetic field, summed in many cases for different site occupancy as

well. Moreover, the high degree of lattice disorder in NCs determines a larger spread of the local crystal-field values at the impurity ions, broadening the EPR spectrum and wiping out spectral features essential in determining the SH parameters. Therefore it is not surprising that previous EPR investigations on nanocrystalline cZnS:Mn (Refs. 8–14) reported a wide range of values for the Mn^{2+} SH parameters. Also, a clear determination of the Mn^{2+} surface center structure, as well as a correlation with the optical emission properties of the host NCs, have not been reported so far.

Recently¹⁵ we reported the accurate determination of the SH parameters for substitutional Mn^{2+} ions in the core of cubic ZnS (cZnS) NCs by a correlated analysis of the low (X -band) and high (W -band) frequency EPR spectra with improved resolution. Our analysis confirmed that, unlike the cZnS single crystals (SC), where the EPR spectra of the substitutional Mn^{2+} ions exhibit cubic symmetry, reflecting the T_d site symmetry of the substituted Zn^{2+} host ion,¹⁶ in the cZnS:Mn NCs such ions are localized at cation sites subjected to a supplementary axial crystal field. Its origin was explained by the preferential localization of the Mn^{2+} ions at cation sites next to an intrinsic extended planar lattice defect, which also seems to play an essential role in the incorporation and stabilization of the Mn^{2+} impurities in the NCs core.

Here we present the results of a combined EPR and luminescence investigation of such small cZnS NCs doped with three concentrations of Mn^{2+} impurity ions, with a narrow size distribution centered at 2 nm, self-assembled into a mesoporous structure. Accurate SH parameters were determined from a quantitative analysis of the EPR spectra recorded at both X (9 GHz) and Q (34 GHz) microwave frequencies for the two surface Mn(II) and Mn(III) centers observed in these NCs,^{14,17} which could be separated by adequate annealing. Based on the comparative analysis of the resulting SH parameters and similar variation of their relative

concentration under thermal treatment with early reported data for Mn^{2+} ions in ZnO NCs, we propose structural models for both Mn(II) and Mn(III) centers involving mixed Mn-O/OH bonding, respectively.

Further on, a comparative analysis of the photoluminescence (PL) (steady state and time resolved) and radioluminescence (RL) data from cZnS:Mn NCs with controlled content of the two surface centers, as well as from cZnS:Mn single crystals, allowed us to distinguish changes in the luminescence properties attributed to the Mn^{2+} impurity ions at substitutional sites in the core of the NCs and to Mn^{2+} ions localized on their surface, or in aggregated states. To the best of our knowledge, it is the first time that such a correlated EPR study of the contained Mn^{2+} -type activating centers and their related luminescence properties in cZnS -doped nanocrystals is reported.

II. EXPERIMENTAL

The manganese-doped nanocrystalline powders of cZnS with a mesoporous structure employed in the present investigation were prepared by precipitation in a surfactant-assisted liquid-liquid reaction, following the procedures reported in Refs. 14 and 17. The preparation started by adding 0.1, 0.2, and 0.5 at. %, respectively, of manganese acetate $[\text{Mn}(\text{CH}_3\text{COO})_2 \cdot 4\text{H}_2\text{O}]$ to the solution of zinc acetate $[\text{Zn}(\text{CH}_3\text{COO})_2 \cdot 2\text{H}_2\text{O}]$, which was mixed for 15 min. The resulting solution was co-precipitated with sodium sulfide $[\text{Na}_2\text{S} \cdot 9\text{H}_2\text{O}]$ in the presence of the Tween 20 (polyoxyethylene sorbitan monolaurate) surfactant. The precipitate was further filtered, washed with bi-distilled water and methanol, and dried at 50°C for 24 h.

According to the structural and morphological x-ray diffraction (XRD) and transmission electron microscopy (TEM) investigations, all samples exhibit a stable mesoporous structure with walls built from NCs of ZnS with a cubic (sphalerite) structure of 2.0 ± 0.3 nm average size and pores of similar size.^{14,15} No significant differences were observed in the size, structure, and morphology of all investigated NCs.

The EPR experiments were performed at room temperature (RT) at the Research Center for Advanced ESR Techniques (CetRESav, <http://cetresav.infim.ro/>) from Magurele-Bucharest. The X-band measurements were performed on a Bruker EMX-plus spectrometer equipped with an E-12 Varian electromagnet. A detailed description of the instrument and magnetic-field calibration procedures were given in Ref. 16. The Q-band EPR measurements were performed with a Bruker ELEXSYS E500Q CW spectrometer. The magnetic-field calibration was made with a BDPA (alpha, gamma-bisdiphenylene-beta-phenyl allyl) reference sample from Bruker, exhibiting a single EPR line with $g = 2.00276$.

The powdery nanocrystalline cZnS:Mn samples were inserted into 3.0- and 1.0-mm-i.d. (inner diameter) sample tubes, respectively, with one end closed, made from pure silica. The thermal treatment of the samples was carried out in air, by inserting the sample tubes into a temperature stabilized ($\pm 1^\circ\text{C}$) furnace for 15 min, at temperatures that were increased in steps of 25°C . After each annealing step, the EPR spectrum was recorded at RT in order to monitor the intensity and/or concentration variation of the Mn^{2+} centers.

The analysis of the resulting EPR spectra, including the determination of the SH parameters and the line-shape analysis by simulations and/or deconvolutions, was performed with the specialized program SIM.^{18,19}

The PL and RL spectra were measured at RT by using an upgraded spectrofluorometer 199S (Edinburgh Instrument) with a TBX-04 (IBH Scotland) photon-counting fast photomultiplier-based detector. A H_2 lamp and an x-ray tube (Mo anticathode, 40 kV, 15 mA) were used as excitation sources, respectively. For decay kinetics measurements, a microsecond pulsed xenon flash lamp was used. The spectra and decays were measured in a 45° geometry (emission from the sample surface). The emission spectra were corrected for the spectral sensitivity of the detection part (single grating emission monochromator coupled to the TBX-04 detector), while the PL excitation (PLE) spectra were corrected for the spectral dependence of the excitation energy given by the H_2 lamp spectrum and the characteristics of the single grating excitation monochromator. The decay curves were approximated by the sum of two to four exponential terms by using the SPECTRASOLVE software (Ames Photonics).

Powdery cZnS:Mn samples were fixed with luminescence-free glue on a black paper support for RL experiments or closed under air in a small metallic cuvette with a quartz window for PL experiments. The cuvette containing the cZnS:0.5\% Mn powder sample was annealed at 200°C for 30 min in a temperature-stabilized furnace.

The PL characteristics of a ZnS SC with a pure cubic structure grown by the gradient technique in PbCl_2 melt, nominally doped with 0.5% MnCl_2 , which was previously characterized by EPR,¹⁶ also have been determined and compared in the same experimental setup with the data from cZnS NCs.

III. RESULTS AND DISCUSSION

A. EPR study

The mesoporous cZnS:Mn samples doped with various Mn^{2+} ion concentrations exhibit EPR spectra similar to those previously reported^{14,20} for the samples doped with 0.2% Mn. They consist of lines from the substitutional Mn(I) and surface Mn(II) and Mn(III) centers (Fig. 1). The transition fields are marked by sets of vertical lines corresponding to the six allowed ($M_S: -1/2 \leftrightarrow 1/2, \Delta M_I = 0$) and ten forbidden ($M_S: -1/2 \leftrightarrow 1/2, \Delta M_I = \pm 1$) central hyperfine transitions for the Mn(I) centers and only six allowed central hyperfine transitions for the Mn(II) and Mn(III) centers.

The EPR linewidth of each center did not change significantly with the manganese doping level, pointing to a high degree of reproducibility in the preparation procedure. Moreover, they vary in the same manner with the microwave frequency, decreasing at higher frequencies. The lines of the substitutional Mn(I) centers, with peak-to-peak linewidth values of $\Delta B(Q) = 0.39$ mT and $\Delta B(X) = 0.48$ mT in the Q- and X-band spectra, respectively, are the narrowest reported so far,^{11,13} pointing to a more reduced degree of lattice disorder in the investigated NCs.

The Mn^{2+} surface centers exhibit microwave saturation properties different from those of the substitutional center.

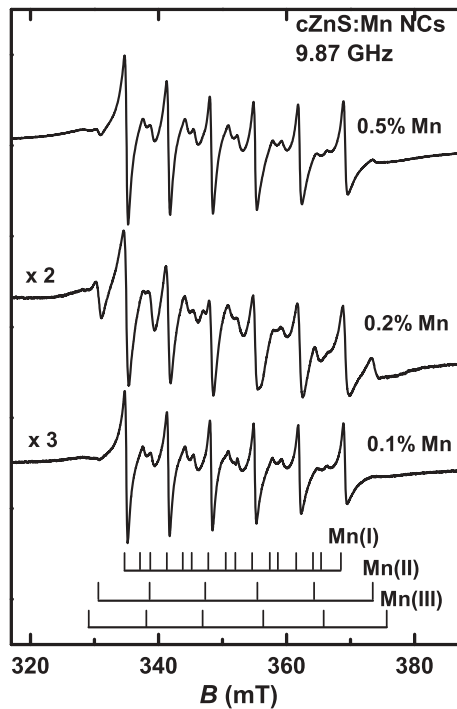


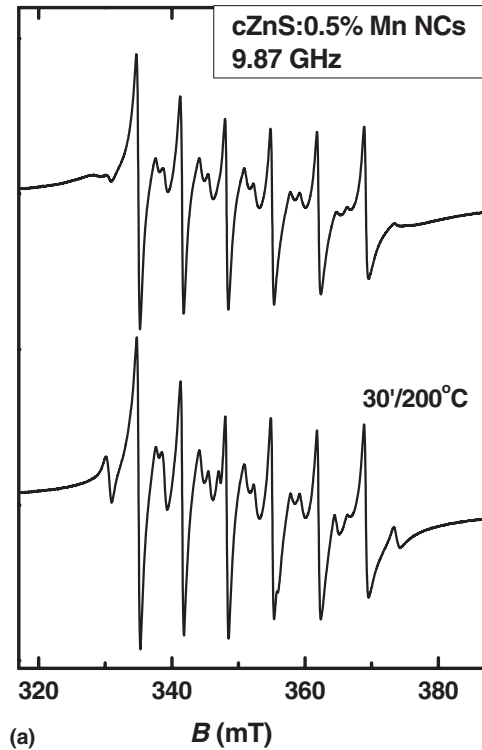
FIG. 1. X-band EPR spectra of mesoporous ZnS doped with various concentrations of manganese. The transition fields marked with vertical lines correspond to each one of the three isolated Mn²⁺ centers.

Thus, in the X-band the hyperfine allowed transitions of the Mn(I) center begin to saturate at microwave power levels of ~0.2 mW, while for the Mn(II) and Mn(III) centers the saturation occurred only at ~2 mW.

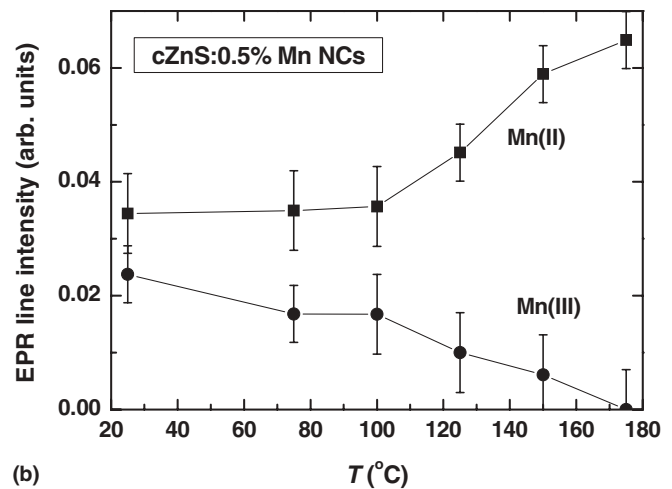
1. Influence of thermal treatments on the EPR spectra

The integrated intensity of the EPR spectrum attributed to substitutional Mn(I) centers in the as-grown samples was found to be proportional with the manganese dopant concentration. At the same time, the relative line intensity of the two surface centers did not show any correlation with the dopant concentration, being sensitive to further thermal treatments. Thus, as shown in Fig. 2(a) in the case of the 0.5% Mn-doped cZnS NCs, the thermal annealing at 200 °C for 30 min resulted in the decay of the Mn(III) spectrum, accompanied by a corresponding increase in the Mn(II) spectrum. Meanwhile, the intensity of the Mn(I) spectrum did not change significantly, as expected for Mn²⁺ ions localized in the core of the cZnS:Mn NCs.

To better understand the temperature effect on the relative concentration of the two manganese surface centers, we submitted cZnS:Mn NCs samples to pulse annealing treatments of 15 min at increasing temperatures and determined their resulting concentration at RT as the EPR line-integrated intensity normalized to the integrated line intensity of the Mn(I) centers. The resulting variation in the concentration of the two surface centers shown in Fig. 2(b) demonstrates that the concentration of the Mn(II) centers increases at the expense of the Mn(III) centers, with their sum being constant. The process is even faster if the sample is annealed



(a)



(b)

FIG. 2. (a) X-band EPR spectra of cZnS NCs doped with 0.5% Mn, as grown, and after 30 min of annealing at 200 °C. (b) The intensity of the Mn(II) and Mn(III) EPR lines vs annealing temperature. The EPR spectra were measured at RT after each 15-min annealing session at increasing temperatures.

in vacuum, the Mn(III) spectrum already decreasing below 100 °C. The results were similar for all three Mn²⁺ doping concentrations. The transformation of the Mn(III) centers into Mn(II) centers was found to be reversible. It was thus possible to prepare samples containing either Mn(I) + Mn(II) centers by annealing at 200 °C, or Mn(I) + Mn(III) centers by storing in ambient atmosphere for a longer period (months). The observed behavior can be explained by considering that both surface centers are Mn²⁺ impurity ions localized on the oxidized surface of the NCs, the Mn(III) center being produced by the reversible adsorption of a neighboring water molecule.

2. *X- and Q-band EPR spectra analysis*

Further information concerning the localization and structure of the observed Mn^{2+} centers resulted from the correlated analysis of the multifrequency (*X*- and *Q*-band) EPR spectra of the cZnS:Mn NCs samples. The EPR spectra of the isolated Mn^{2+} ($3d^5$) ions are described by the following spin Hamiltonian for cubic symmetry with the usual notations,²¹ to which a small axial distortion was added:

$$H = \mu_B \mathbf{S} \cdot \mathbf{g} \cdot \mathbf{B} + \mathbf{S} \cdot \mathbf{A} \cdot \mathbf{I} + \frac{a}{6} \left[(S_\xi^4 + S_\eta^4 + S_\zeta^4) + \frac{1}{5} S(S+1)(3S^2 + 3S - 1) \right] + D \left[S_z^2 - \frac{1}{3} S(S+1) \right] + \mu_N g_N \mathbf{B} \cdot \mathbf{I}. \quad (1)$$

Here the first two terms represent the main interactions of the $S = 5/2$ electron spin with the external magnetic field and with the $I = 5/2$ nuclear spin of the ^{55}Mn (100% abundance) isotope, respectively. The next two zero-field splitting (ZFS) terms describe the interaction of the electron spin with the local cubic crystal field characterized by the cubic ZFS parameter a and by a perturbing axial crystal field characterized by the D parameter. The last term in Eq. (1) corresponds to the nuclear Zeeman interaction of the $I = 5/2$ spin with the external magnetic field. The (x, y, z) coordinates refer to the axial component of the crystal field, while the (ξ, η, ζ) coordinates refer to the cubic component of the crystal field. In the case of cubic ZnS single crystals, the axial fine structure parameter D vanishes and (x, y, z) become the cubic axes.

Accurate SH parameter values can be obtained by a correlated quantitative analysis of the low- and high-frequency EPR spectra in a two-step procedure, already employed for the analysis of the EPR spectra of the substitutional Mn(I) centers.¹⁵ Thus, in the first step, accurate g - and A -parameter values are obtained by fitting the line positions in the high-frequency EPR spectrum with the calculated spectra considering only the electronic Zeeman and hyperfine interactions. Perturbation calculations up to the third order have shown²² that in the powder spectra of the Mn^{2+} ions the positions of the allowed and forbidden central transitions are influenced by the axial ZFS term only in the second ($\sim D^2/B$) and third ($\sim AD^2/B^2$) approximations. Therefore, for both *W*- and *Q*-band spectra, the effect of the ZFS terms of moderate magnitude ($|D| < 50 \times 10^{-4} \text{ cm}^{-1}$) on both line positions and line shape of the allowed and forbidden central transitions is comparable to the experimental errors. Moreover, the increased g resolution at higher magnetic field and/or frequency reduces the overlap of the Mn(I) spectrum with the lines of the Mn(II) and Mn(III) centers, increasing the accuracy in determining the transition fields.

In the second step, the resulting g - and A -parameter values are used as fixed values in determining the ZFS parameters by fitting both *X*- and *Q*-band experimental spectra with computed line-shape simulations that take into account, besides the spatial averaging, local strain broadening effects and the forbidden hyperfine transitions. This procedure increases the accuracy in determining the D -parameter value because it includes as experimental fitting data, besides the central line positions, the line shape of the central hyperfine

forbidden transitions. The line broadening, which was found to occur even for the high-quality cubic ZnS crystals,¹⁶ is associated with fluctuations in the local crystal field at the Mn^{2+} ion determined by the presence of defects and local lattice strains.²³ These fluctuations are reflected in variations of the SH parameters that are most affected by the local environment, i.e., the ZFS parameters.

In determining the SH parameters of the Mn^{2+} surface centers, we have employed the experimental spectra recorded for samples annealed at 200 °C, containing only Mn(I) and Mn(II) centers, and from aged samples, containing mainly Mn(I) and Mn(III) centers. Accurate g - and A -parameter values were determined for the Mn(II) and Mn(III) centers from the *Q*-band spectra (Table I). However, because the forbidden transitions in the *X*-band spectrum could not be observed in either case owing to the larger linewidth and the overlap of the more intense Mn(I) spectrum, we could only determine a range of values for the axial D parameter for which the line shape of the allowed transitions remained undistorted, reproducing well the experimental *X*-band spectrum.

The resulting *X*- and *Q*-band spectrum simulations are compared in Figs. 3(a) and 3(b), respectively, with the experimental spectra of the 0.2% Mn-doped ZnS NCs containing all Mn^{2+} centers. For the Mn(I) centers we used the earlier determined SH parameters¹⁵ (Table I). The line broadening effects were reproduced by including Gaussian distributions of the ZFS parameter values, centered on the $a = 7.987 \times 10^{-4} \text{ cm}^{-1}$ and $|D| = 41 \times 10^{-4} \text{ cm}^{-1}$ values, with standard deviations of $\sigma(a) = 0.8 \times 10^{-4} \text{ cm}^{-1}$ and $\sigma(D) = 15 \times 10^{-4} \text{ cm}^{-1}$. The best fit was obtained for a Lorentzian line shape, with peak-to-peak linewidths of $\Delta B(X) = 0.48 \text{ mT}$ and $\Delta B(Q) = 0.39 \text{ mT}$ for the *X*- and *Q*-band spectra, respectively. The resulting broadening parameter values, one order of magnitude larger compared to the manganese-doped cZnS single crystals,¹⁶ reflect the higher degree of lattice disorder in the nanocrystals.

For the two surface centers, the Lorentzian line-shape simulations were performed with the following parameters: $|D| = 70 \times 10^{-4} \text{ cm}^{-1}$, $\sigma|D| = 40 \times 10^{-4} \text{ cm}^{-1}$, $\Delta B(X) = 0.85 \text{ mT}$, and $\Delta B(Q) = 0.7 \text{ mT}$ values for the Mn(II) center and $|D| = 80 \times 10^{-4} \text{ cm}^{-1}$, $\sigma|D| = 50 \times 10^{-4} \text{ cm}^{-1}$, and $\Delta B(X) = \Delta B(Q) = 1.5 \text{ mT}$ values for the Mn(III) center. As expected, the fluctuations in the local crystal field at the surface are considerably larger than in the core of the NCs.

One should mention the presence in the *X*-band spectra of a broad ($\Delta B \sim 29 \text{ mT}$) line centered at $g = 2.003$, attributed to aggregates of the manganese ions. Their contribution was included in the *X*-band spectrum simulations as a Lorentzian-shaped line with the above-mentioned parameters. A similar EPR signal was previously observed in the EPR spectra of cZnS polycrystalline powders doped with high concentrations of manganese.²⁴ Because its intensity varied from sample to sample, we attribute it to residues of the doping process, in the form of manganese compounds (manganese acetate and/or manganese sulfide) dispersed between the cZnS:Mn NCs.

3. *Structure of the Mn^{2+} centers in the cZnS nanocrystals*

Structural models for the two surface Mn^{2+} centers observed in our nanocrystalline cZnS:Mn samples can be

TABLE I. Spin Hamiltonian parameters at RT attributed to Mn²⁺ centers in nanocrystalline cZnS and in various ZnO and Zn(OH)₂ structures. The EPR linewidth (ΔB) and the measuring EPR microwave band are also mentioned where available.

Lattice host/Mn ²⁺ center	g	A (10 ⁻⁴ cm ⁻¹)	ZFS (10 ⁻⁴ cm ⁻¹)	ΔB (mT)
Nano cZnS:Mn/Mn(I) ^a	2.0022 ± 0.0001	-63.70 ± 0.05	D = 41 ± 3 a = 7.987	0.48 (X), 0.39 (Q), 0.36 (W)
Nano cZnS:Mn/Mn(II) ^b	2.0012 ± 0.0002	-80.5 ± 0.1	D = 10–80	0.85 (X), 0.7 (Q)
Nano cZnS:Mn/Mn(III) ^b	2.0009 ± 0.0002	-86.8 ± 0.5	D = 10–90	1.5 (X), 1.5 (Q)
Nano cZnS:Mn/agglomerated Mn ^b	2.003			29 (X)
Nano cZnS:Mn/II ^c	g_{\perp} = 2.006 g_{\parallel} = 2.003	A_{\perp} = -79.5 A_{\parallel} = -84.0	D = 373.9 $ E $ = 124.6	4.8 (X)
Nano cZnS:Mn/SD ^c	g_{\perp} = 2.006 g_{\parallel} = 2.003	A_{\perp} = -79.5 A_{\parallel} = -84.0	D = 140.2 $ E $ = 46.7	4.8 (X)
Nano cZnS:Mn/signal II ^d	2.0013	-84.13	D = 160.0	1.08 (Q)
Nano cZnS:Mn/NC2 ^e	2.001	-89	D = 500 – 1000	
Nano ZnS:Mn/S _{II} ^f	2.001	-90		4.7 (X)
Nano cZnS:Mn-sample 3/surface Mn ^{2+g}	2.002	-105.0		
ZnO:Mn single crystal/substitutional Mn ^{2+h}	2.0012	-73.38	D = -225.2 $a - F$ = 5.5	
Nano ZnO:Mn/substitutional SI ⁱ	2.0028	-74.6		
Zn(OH) ₂ shell of ZnO:Mn NCs/surface SII ⁱ	2.001	-89		
Powder Zn(OH) ₂ /substitutional Mn ²⁺ⁱ	2.001	-89		

^aReference 15.

^bThis work.

^cReference 13.

^dReferences 10 and 11.

^eReference 9.

^fReference 8.

^gReference 12.

^hReference 26.

ⁱReference 25.

inferred from the results of the EPR investigations. Table I lists, besides the SH parameters of the Mn²⁺ centers observed in our NCs samples, the SH parameters of the surface

centers previously reported in cZnS:Mn NCs, as well as of the Mn²⁺ centers reported in various ZnO and Zn(OH)₂ structures. The Mn(II) and Mn(III) centers exhibit g -parameter values and hyperfine A -parameter values close to those of the corresponding SI and SII centers reported in ZnO:Mn NCs.²⁵ These last two centers exhibit similar SH parameter values with those of the substitutional Mn²⁺ ions in crystalline ZnO (Ref. 26) and Zn(OH)₂,²⁵ respectively, which lead to the identification of the SI centers as substitutional Mn²⁺ ions localized in the core of the ZnO NCs, and of the SII centers as Mn²⁺ ions situated on the surface of the ZnO NCs, covered by a Zn(OH)₂ layer. It was also observed that under thermal treatment in air, up to 200 °C, the concentration of the SII centers decreased, while the concentration of the SI centers increased (see Fig. 5 of Ref. 25), a process which was attributed to the thermal decomposition of Zn(OH)₂ into ZnO.

Based on the similar SH parameter values and behavior under thermal annealing with the SI and SII centers in ZnO:Mn NCs, one concludes that the Mn(II) centers represent Mn²⁺ ions localized in oxidized areas of the cZnS:Mn NCs's surface. During the aging process such areas adsorb atmospheric water molecules, resulting in Mn(III) centers, i.e., Mn²⁺ ions localized in hydrolyzed areas with a Zn(OH)₂ structure formed onto the NCs's surface. The proposed structural models also explain the larger A -parameter values of both Mn(III) and Mn(II) surface centers with respect to the substitutional Mn(I) centers, as resulting from changes in the nature of the bonding, from Mn-S to the more ionic Mn-O/OH.²⁷ In line with this

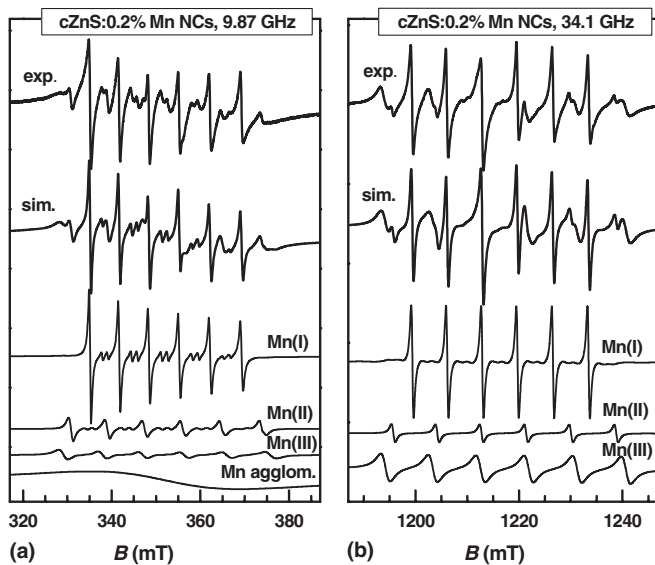


FIG. 3. EPR spectra of cZnS NCs doped with 0.2% Mn measured in the (a) X and (b) Q microwave frequency bands (exp.) and the simulated spectra (sim.) obtained as a summation of the simulated spectra of the observed Mn²⁺ centers (lower spectra), calculated with the spin Hamiltonian parameters from Table I.

reasoning, the differences between the A -parameter values of the corresponding surface centers in the cZnS and ZnO NCs may be due to a mixed Mn-S-O/OH bonding at the surface of the cZnS NCs, as compared to the Mn-O/OH bonding in the ZnO NCs.

Based on the close SH parameter values previously reported for the Mn^{2+} surface centers in cZnS NCs (Table I), it seems very likely that the SII centers reported by Igarashi *et al.*^{10,11} also represent Mn^{2+} ions in the oxidized areas at the surface of the cZnS NCs, similar to the Mn(II) centers. Also, the NC2 centers reported by Kennedy *et al.*⁹ and the SII centers reported by Borse *et al.*⁸ (Table I) are very likely Mn^{2+} ions in hydrolyzed surface areas of the cZnS NCs, similar to the Mn(III) centers.

B. The luminescence investigations

Luminescence investigations were carried out in a quest to separate the contributions to luminescence from the substitutional and surface Mn^{2+} centers. The investigations were carried out on the as-grown 0.1%, 0.2%, and 0.5% Mn-doped cZnS and 0.5% Mn-doped cZnS annealed for 30 min at 200 °C nanocrystalline samples. From the EPR spectra in Fig. 1, one can see that the 0.1% Mn-doped cZnS NCs contain, besides the substitutional Mn(I) centers, mainly Mn(III) surface centers. Meanwhile, in the annealed 0.5% Mn-doped sample all surface centers are of Mn(II)-type. In order to determine the possible presence of size-related effects, similar optical measurements were carried out on a Mn^{2+} -doped ZnS high-quality single crystal with a pure cubic structure. According to detailed EPR investigations, the Mn^{2+} impurity ions in this cZnS:Mn single crystal are localized substitutionally, at cation Zn^{2+} sites with local T_d symmetry.¹⁶ To the best of our knowledge it is the first time that such investigations are reported, in which the presence and localization of the Mn^{2+} ions have been accurately determined by EPR spectroscopy.

1. Radioluminescence

The RL spectra of the as-grown 0.1% and 0.5% Mn-doped nanocrystalline cZnS samples, as well as of a reference cZnS:Mn single crystal, are displayed in Fig. 4. The two nanocrystalline sample spectra consist of two broad bands, one centered at 450 nm and one centered at 605 nm. The first one can be related to the blue emission centered at ~ 435 nm, termed “self-activated,” which has been previously reported in micrometer-sized cubic ZnS particles and attributed to the recombination at crystal lattice defects (sulfur²⁸ or zinc^{29,30} vacancies). The absolute intensity of the emission at 605 nm from the Mn^{2+} ions is higher for the 0.5% Mn-doped sample, while the intrinsic emission at 450 nm is comparatively weaker than for the 0.1% Mn-doped sample. This effect can be well explained by the competition for charge-carrier capture at the ZnS lattice and Mn^{2+} centers.²⁸

The RL spectrum of the cZnS:Mn SC has almost no contribution from the lattice defects, reflecting the low defect content and insignificant role of the surface defects.³¹ The Mn^{2+} orange emission is narrower and more symmetric than for the nanocrystalline samples, being centered at 585 nm, similar with earlier observations on micrometer-sized cZnS:Mn phosphors.²⁸

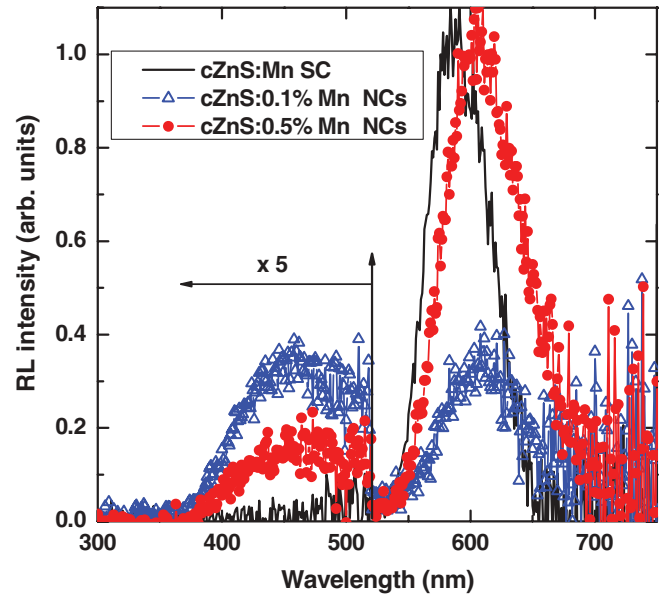


FIG. 4. (Color online) RL spectra of the as-grown 0.1% Mn (triangles) and 0.5% Mn (circles) doped cZnS NCs and the cubic ZnS : Mn SC (solid line).

2. Steady-state photoluminescence

The emission spectra of the NCs have been recorded at excitation wavelengths corresponding to the excitonic and band-gap absorption of the cZnS nanopowders (330–340 nm) (Fig. 5). The emission spectra of the cZnS NCs doped with 0.1%, 0.2%, and 0.5% Mn consist of the dominant broad band peaking at 605 nm from the Mn^{2+} ions and the host lattice emission peaking at ~ 440 nm. The relative intensity of the host emission decreases with an increase in the nominal Mn concentration, almost completely disappearing for the 0.5% Mn-doped sample.

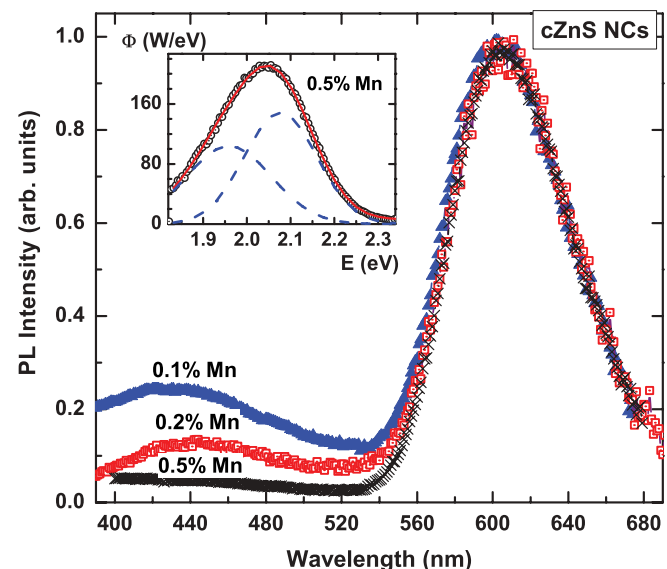


FIG. 5. (Color online) Emission spectra measured on the 0.2% Mn-doped ZnS NCs for the 340-nm excitation wavelength and on the 0.1% and 0.5% Mn-doped ZnS NCs for the 330-nm excitation wavelength, respectively. Inset: Gaussian decomposition of the orange emission band of the 0.5% Mn-doped ZnS NCs.

Mn-doped sample, which is consistent with the RL spectra and the concept of competition for charge-carrier capture at the host lattice and Mn²⁺ centers. The emission spectrum of the 0.5% Mn-doped cZnS NCs sample does not change after annealing.

The decomposition of the Mn²⁺ emission band using a Gaussian fit resulted in two peaks centered at 2.08 eV (~596 nm) and 1.96 eV (~632 nm) (Fig. 5 inset). The full width at half maximum of the resulting subbands are 0.20 and 0.23 eV, respectively. Their positions were found to be insensitive to both doping level and changes in the relative concentration of the two surface Mn(II) and Mn(III) centers. The 596-nm band, ascribed to the ⁴T₁–⁶A₁ transition of the Mn²⁺ impurity ions, has a ~9-nm redshift relative to the cZnS:Mn single crystal, in agreement with previous reports.^{2–5,28} Its insensitivity to both manganese doping levels and relative concentration of the two Mn²⁺ surface centers strongly suggests that it originates from manganese ions localized at the core of the NCs, in agreement with the observations of Sooklal *et al.*⁵ They also concluded that the surface bound Mn²⁺ ions contribute only to the quenching of the intrinsic defect emission and the promotion of the near band-gap emission in UV.

Regarding the 630-nm band, a similar lower-energy band has been previously observed in cZnS:Mn NCs doped with high Mn concentrations.³² Bulanyi *et al.*³³ have also reported in highly defective manganese-doped cZnS crystals an emission band peaking at 637 nm, which they attributed to a separate phase of α-MnS. We also consider that the observed 630-nm component band is very likely due to the aggregated manganese ions, resulting in the broad EPR line observed in the X-band spectra.

The excitation (PLE) spectrum for the 450-nm host emission consists of a single band centered at ~337 nm. The PLE spectra for the Mn²⁺ emission measured at 570 and 600 nm in the as-grown 0.5% Mn-doped ZnS NCs are shown in Fig. 6(a). Two excitation bands can be resolved: (i) one band corresponding to the cZnS band-gap transition,

centered at ~335 nm, in which both the host (λ_{em} = 450 nm) and Mn²⁺ (λ_{em} = 600 nm) emissions are excited; and (ii) a lower intensity band at ~345 nm [marked with an arrow in Fig. 6(a)]. The latter band was obtained by the subtraction of the PLE spectra for the 600- and 570-nm emissions. In the case of the annealed 0.5% Mn-doped cZnS NCs, the PLE spectra recorded at the two emission wavelengths were identical.

Figure 6(b) displays the PLE spectra for the 600-nm emission measured on the as-grown and annealed 0.5% Mn-doped cZnS NC sample. The two spectra could be made equal within the 250–330 nm range owing to their identical shape in this region, the as-grown spectrum being further subtracted from the spectrum of the annealed sample. The resulting difference spectrum consists of a band centered at 360 nm (marked with an arrow), which therefore is related with recombination centers whose concentration increases after the annealing-induced water desorption. A correlation with the results of EPR measurements strongly suggests that the excitation band at 360 nm can be associated with the Mn(II) centers. Similarly, the excitation band at 345 nm can be associated with the Mn(III) centers, which are dominant in the as-grown samples and are bleached out by annealing. As no clear contribution from the Mn(II) and Mn(III) centers was found in the emission spectra (see above), it is likely that these centers may just transfer the absorbed energy to the substitutional Mn²⁺ ions in the core of the NCs.

The PL excitation and emission spectra of the cZnS:Mn SC are displayed in Fig. 7. The PLE spectrum of the Mn²⁺ emission, measured for the 585-nm emission wavelength, shows clearly an excitation band at ~330–340 nm, which corresponds to the one found for the cZnS:Mn NCs and is related to the excitonic (or band-to-band) transition of the cZnS host. The broad bands at ~390 and 440 nm are related to the Mn²⁺ transitions into the higher energy ⁴T₁(⁴P) and ⁴T₂(⁴D) levels, respectively, of the Mn²⁺ (3d⁵) configuration.³⁴ The pronounced differences in the single-crystal excitation spectrum with respect to the nanopowder can be explained easily by

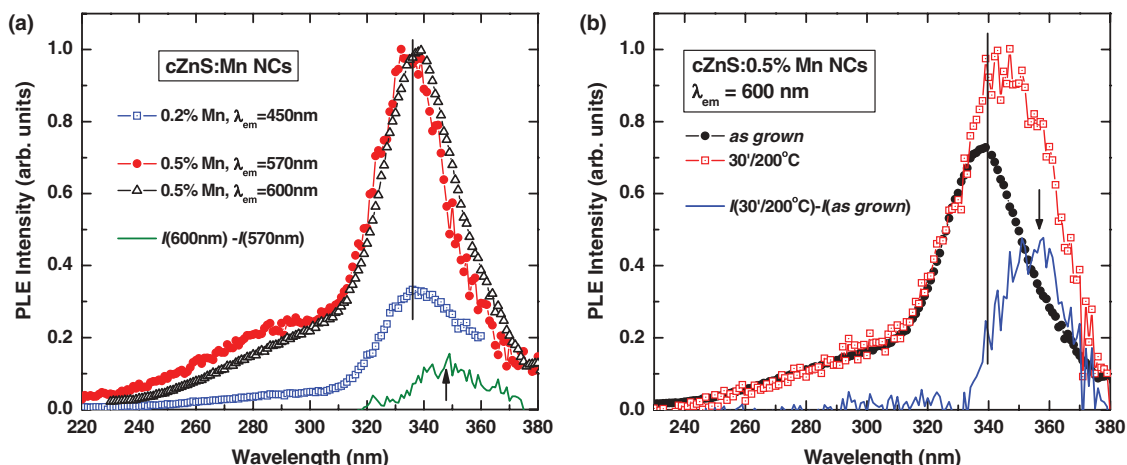


FIG. 6. (Color online) (a) Excitation spectra measured on the as-grown 0.2% Mn-doped ZnS NCs for the 450-nm emission and as-grown 0.5% Mn-doped ZnS NCs for the 570- and 600-nm emission wavelengths, respectively. The difference between the PLE spectra measured for the 570- and 600-nm emissions appears as a small band shifted to longer wavelengths, marked by the arrow. (b) Excitation spectra for the as-grown and annealed 0.5% Mn-doped ZnS NCs and their difference spectrum after spectra equalization within the 250–330 nm range.

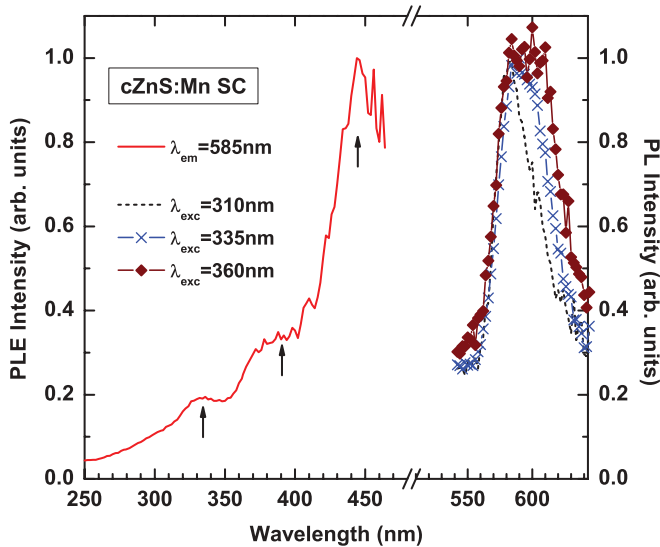


FIG. 7. (Color online) Excitation and emission spectra of the cZnS:Mn SC.

the enabled direct excitation of the Mn^{2+} centers in optically thick samples.^{35,36}

The increase of the excitation wavelength from 310 to 360 nm results in the broadening of the emission band toward the lower-energy side (Fig. 7). The emission band at ~ 580 nm thus can be related to the substitutional cubic Mn^{2+} centers, a result also obtained on micrometer-sized cZnS:Mn phosphors,²⁸ while the emission at approximately and beyond 600 nm seems very likely to be due to perturbed Mn^{2+} centers. In our sample such centers could be pairs of Mn^{2+} ions, whose presence was manifested in the EPR spectra as a dipolar line broadening.¹⁶

3. Decay kinetics of Mn^{2+} photoluminescence

Time-resolved PL investigations were performed on the as-grown 0.1% and 0.5% doped cZnS:Mn nanocrystalline samples, on the 0.5% doped nanocrystalline sample annealed in air at 200 °C, and on the cZnS:Mn single crystal.

a. The Mn-doped cZnS nanocrystals. The Mn^{2+} emission decay times of the 0.1% Mn and 0.5% Mn-doped cZnS NCs were measured for the 590–600 nm emission wavelengths and the 330-, 360-, and 450-nm excitation wavelengths. The decays were generally nonexponential and could be approximated by the sum of three to four exponentials, as shown in Fig. 8. In the tail of the decay, characteristic decay times within the 3.3–4.1 ms range were obtained from the fit, longer than the usual 1.8–1.9 ms values previously obtained for cZnS:Mn NCs.³ The components with decay times of the order of 10^{-2} , 10^{-1} , and 1 ms are further denoted as fast, medium, and slow components, respectively.

The wavelength dependence of the resulting decay times, determined across the Mn^{2+} emission band, are given for the as-grown [Fig. 9(a)] and annealed [Fig. 9(b)] 0.5% Mn-doped sample, respectively, at 330-, 360-, and 450-nm excitation wavelengths. The wavelength dependence curves of the as-grown sample are less flat than in the case of the 0.1% Mn^{2+} -doped NCs, especially in the outer regions, which could

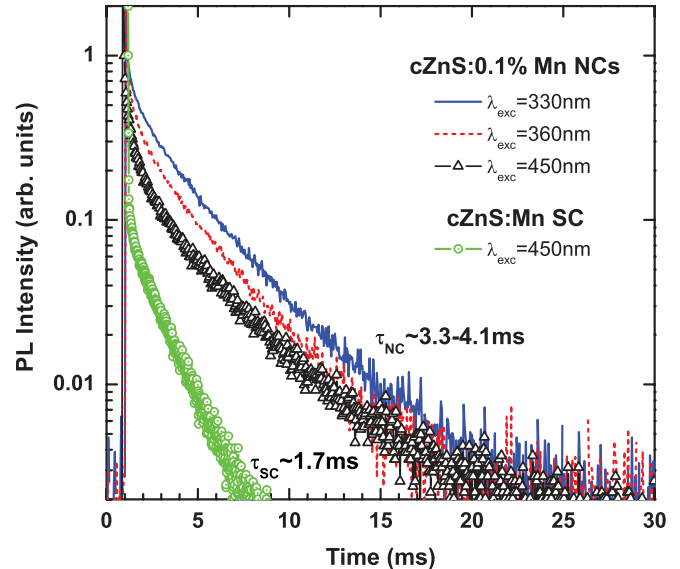


FIG. 8. (Color online) Normalized PL decay curves of the Mn^{2+} emission ($\lambda_{\text{em}} = 590$ nm) of the 0.1% Mn-doped cZnS NC sample for the 330-, 360-, and 450-nm excitation wavelengths and of the bulk sample for the 450-nm excitation.

be explained by a higher occurrence of distorted centers or possibly Mn pairing. The slow and medium decay components are indeed in the range of values (1 and 10^{-1} ms, respectively) previously observed for single and pairs of Mn^{2+} ions in ZnS NCs, respectively.^{37,38} The decays are accelerated under the 360-nm excitation and are markedly nonexponential under the 450-nm excitation.

After annealing the 0.5% Mn-doped cZnS NCs in air at 200 °C for 30 min, the observed wavelength dependence of the decay time becomes flatter for the dominant (medium and slow) intensity components [Fig. 9(b)]. This behavior shows that the emission centers become structurally more uniform, which can be related with the bleaching out of the Mn(III) centers and therefore the involvement of only one type of surface center, namely Mn(II), in the pair interactions.

The fast drop in the decay time values for emission wavelengths larger than 630 nm, observed in all samples, is attributed to the involvement of the manganese aggregates in the PL process.

b. The ZnS:Mn single crystal with a pure cubic structure. Similar PL decay measurements were also performed on a cZnS:Mn single crystal estimated from EPR measurements¹⁴ to contain ~ 200 ppm Mn^{2+} ions. Contrary to the nanocrystalline powder samples, in the SC the 450-nm excitation results in a more single-exponential-like decay (see Fig. 8), as expected from the dominant presence of only one type of Mn^{2+} center (substitutional Mn^{2+} ions at T_d sites).

The wavelength dependence of the decay times throughout the Mn^{2+} emission band is presented in Fig. 10. It shows relatively flat dependences, which points to the uniformity of the emission centers. The values of the slowest component decay time of 1.7–1.8 ms, similar to previous reports,³⁹ are distinctly shorter with respect to the powder samples. Even the medium and fast components of the decay times are slightly shorter than in the NCs. The range of values obtained are

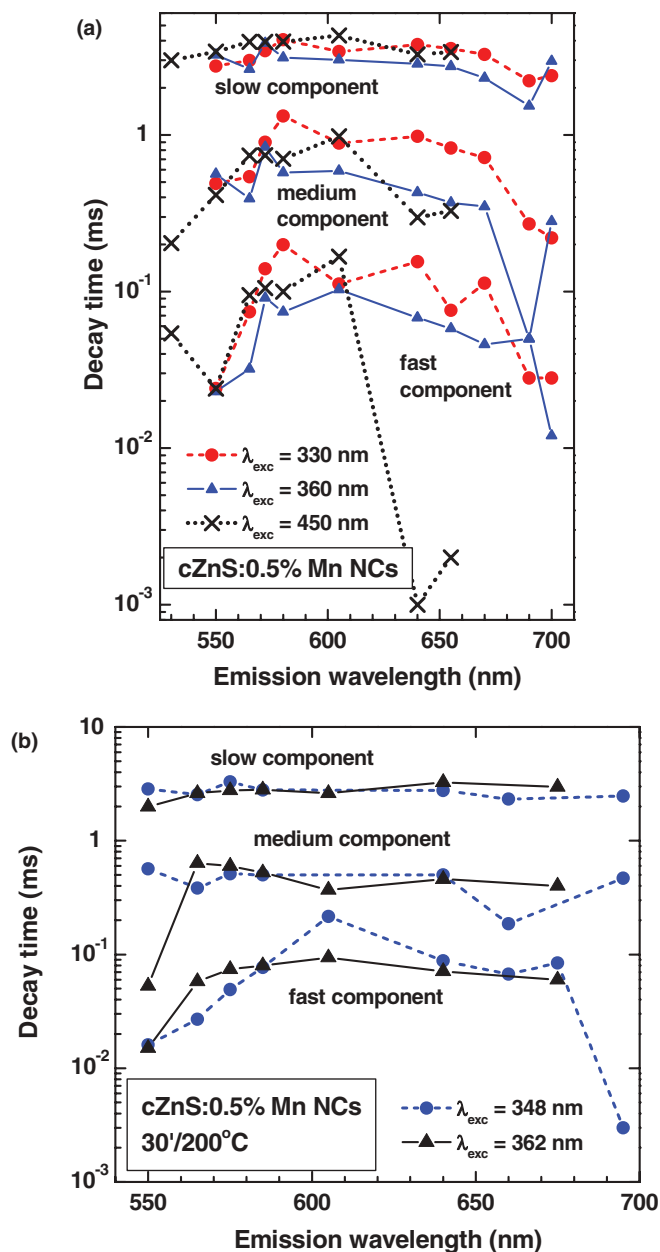


FIG. 9. (Color online) Wavelength dependence of the component decay times of the Mn²⁺ emission (a) for the as-grown 0.5% Mn-doped cZnS NC sample obtained from the decay approximations at 330-, 360-, and 450-nm excitation wavelengths, and (b) for the same sample annealed for 30 min at 200 °C at the 348- and 362-nm excitation wavelengths.

similar as order of magnitude to the decay times reported by Busse *et al.*⁴⁰ and attributed to single Mn²⁺ ions (slow), near-next-neighboring pairs of Mn²⁺ ions (medium), and next-neighboring pairs of Mn²⁺ ions (fast).

Returning to the NC samples, we could attribute the two submillisecond components of the decay times to pairs of Mn²⁺ ions separated by different distances. Considering the doping levels and the small sizes of our investigated NCs, only one or two Mn²⁺ ions at most can be present on the average in the core of the NCs, and such a pair most probably involves Mn²⁺ ions from the core and surface of the NCs.

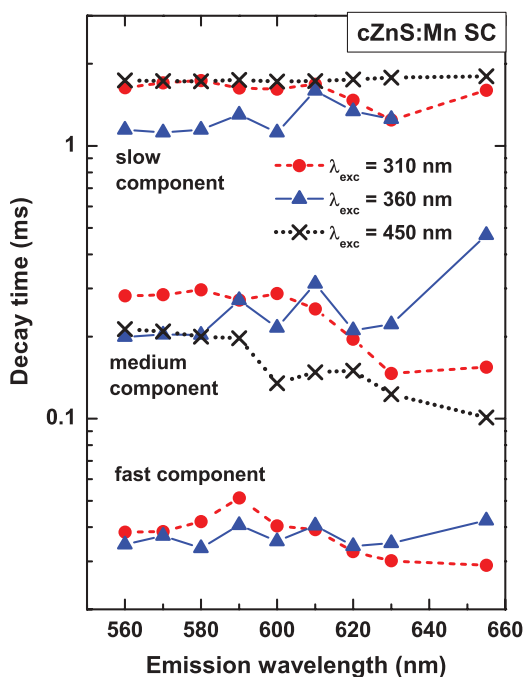


FIG. 10. (Color online) Wavelength dependence of the component decay times of the Mn²⁺ emission (λ_{em} = 590 nm) in cubic ZnS:Mn SC calculated from the decay approximations.

The systematically longer decay times of the Mn²⁺ centers in nanocrystals compared to those measured in the single crystal can be understood in the following way: It has been shown in literature⁴¹ that in small enough nanocrystals the lifetimes τ_R of the emission centers are getting longer owing to the dependence of τ_R on the inverse fifth power of the refractive index. If the refractive index of the surrounding medium is smaller than that of the nanocrystals (e.g., nanocrystals in air), a lengthening of τ_R will be observed due to the “filling effect,” i.e., owing to the fact that the active sample volume includes partially the surrounding medium.

IV. CONCLUSIONS

Our combined X- and Q-band EPR study has revealed the presence in the cZnS nanocrystals doped with 0.1%, 0.2%, and 0.5% Mn²⁺ ions of three types of isolated Mn²⁺ ions localized at different sites in the nanocrystals, called Mn(I), Mn(II), and Mn(III) centers. Aggregates of residual manganese ions have been observed also as a broad band in the X-band EPR spectra. As demonstrated in a previous EPR and high-resolution TEM (HRTEM) study,¹⁵ the Mn(I) centers consist of Mn²⁺ ions localized substitutionally in the cZnS NCs’s lattice core, at Zn²⁺ sites next to a stacking defect that determines an additional axial local crystal field characterized by the ZFS parameter |D| = 41 × 10⁻⁴ cm⁻¹.

We have shown here that the other two Mn(II) and Mn(III) centers, with different spin Hamiltonian parameters (Table I), correspond to Mn²⁺ ions at the surface of the cZnS NCs in oxidized and hydrolyzed areas, respectively. Although their total concentration with respect to the Mn(I) center concentration remains constant, their relative concentration depends

on the thermal history of the sample. Based on a comparative analysis of their SH parameters and production properties with similar centers in ZnO and Zn(OH)₂ nanocrystals^{25,26}, it is suggested that the Mn(II) centers are very likely Mn²⁺ ions localized in oxidized areas of the cZnS:Mn NCs's surface, characterized by mixed Mn-O-S bonding, while the Mn(III) centers are Mn²⁺ ions in areas on the cZnS NCs, characterized by mixed Mn-O-OH bonding.

From the steady-state and time-resolved PL measurements it follows that the intense broad band peaking at ~605 nm in the cZnS NCs can be decomposed in two components peaking at 596 and 630 nm, respectively, whose position did not vary with the doping level or relative concentration of the two surface Mn²⁺ centers. The band centered at 596 nm was assigned to the ⁴T₁–⁶A₁ transition of the Mn²⁺ ions localized in the NCs's core, therefore to the Mn(I) centers. The 630-nm band has been attributed to the residual Mn²⁺-based aggregates observed by EPR.

The analysis of the excitation spectra recorded for the substitutional Mn²⁺ ions emission reveals the presence of two bands at 345 and 360 nm, whose evolution under annealing is correlated with that of the two Mn(III) and Mn(II) surface centers, respectively.

The decay time measurements on the NC samples evidenced the presence of two submillisecond components, besides the expected millisecond component characteristic to Mn²⁺ localized substitutionally in Zn²⁺ sites in the cZnS NCs. From the analysis of the spectral distribution of the decay times and the comparison with the single-crystal results, we concluded that these two faster components can be ascribed to a pair of Mn²⁺ ions, the constituents of which are most likely localized in the core and shell of the same nanocrystal. The longer decay times of the Mn²⁺-related centers in nanocrystals compared to those measured in the single crystal are explained by the “filling effect” in small enough nanocrystals, in which the active sample volume includes partially the surrounding medium.

ACKNOWLEDGMENTS

This work was supported by CNCISIS-UEFISCSU, project number PN-II-IDEI-523/2008. The authors are grateful to Leona C. Nistor and Ruxandra Birjega for the structural (TEM and XRD, respectively) characterization of the investigated cZnS:Mn nanocrystalline samples. Financial support from the Czech GA AV KAN300100802 project is also gratefully acknowledged.

-
- ¹H. Hu and W. Zhang, *Opt. Mater.* **28**, 536 (2006), and references therein.
- ²R. N. Bhargava, D. Gallagher, X. Hong, and A. Nurmikko, *Phys. Rev. Lett.* **72**, 416 (1994).
- ³A. A. Bol and A. Meijerink, *Phys. Rev. B* **58**, R15997 (1998); *J. Phys. Chem. B* **105**, 10197 (2001).
- ⁴M. Tanaka, J. Qi, and Y. Masumoto, *J. Lumin.* **87–89**, 472 (2000).
- ⁵K. Sooklal, B. C. Cullum, S. M. Angel, and C. J. Murphy, *J. Phys. Chem.* **100**, 4551 (1996).
- ⁶M. W. Porambo and A. L. Marsh, *Opt. Mater.* **31**, 1631 (2009).
- ⁷J. R. Pilbrow, *Transition Ion Electron Paramagnetic Resonance* (Clarendon, Oxford, 1990).
- ⁸P. H. Borse, D. Srinivas, R. F. Shinde, S. K. Date, W. Vogel, and S. K. Kulkarni, *Phys. Rev. B* **60**, 8659 (1999).
- ⁹T. A. Kennedy, E. R. Glaser, P. B. Klein, and R. N. Bhargava, *Phys. Rev. B* **52**, R14356 (1995).
- ¹⁰T. Igarashi, T. Isobe, and M. Senna, *Phys. Rev. B* **56**, 6444 (1997).
- ¹¹T. Igarashi, M. Ihara, T. Kusunoki, K. Ohno, T. Isobe, and M. Senna, *J. Nanopart. Res.* **3**, 51 (2001).
- ¹²P. A. Gonzales Beermann, B. R. Mc Garvey, S. Muralidharan, and R. C. W. Sung, *Chem. Mater.* **16**, 915 (2004).
- ¹³P. A. Gonzales Beermann, B. R. Mc Garvey, B. O. Skadtchenko, S. Muralidharan, and R. C. W. Sung, *J. Nanopart. Res.* **8**, 235 (2006).
- ¹⁴S. V. Nistor, L. C. Nistor, M. Stefan, C. D. Mateescu, R. Birjega, N. Solovieva and M. Nikl, *Superlattices Microstruct.* **46**, 306 (2009).
- ¹⁵S.V. Nistor, M. Stefan, L. C. Nistor, E. Goovaerts, and G. Van Tendeloo, *Phys. Rev. B* **81**, 035336 (2010).
- ¹⁶S.V. Nistor and M. Stefan, *J. Phys. Condens. Matter* **21**, 145408 (2009).
- ¹⁷L. C. Nistor, C. D. Mateescu, R. Birjega, and S. V. Nistor, *Appl. Phys. A* **92**, 295 (2008).
- ¹⁸J. Glerup and H. Weihe, *Acta Chem. Scand.* **45**, 444 (1991).
- ¹⁹C. J. H. Jacobsen, E. Pedersen, J. Villadsen, and H. Weihe, *Inorg. Chem.* **32**, 1216 (1993).
- ²⁰S.V. Nistor, M. Stefan, L. C. Nistor, C. D. Mateescu, and R. Birjega, *J. Nanosci. Nanotechnol.* **10**, 6200 (2010).
- ²¹A. Abragam and B. Bleaney, *Electron Paramagnetic Resonance of Transition Ions* (Clarendon, Oxford, 1970).
- ²²A. Nicula, I. Ursu, and S. V. Nistor, *Rev. Roum. Phys.* **10**, 229 (1965).
- ²³A. M. Stoneham, *Rev. Mod. Phys.* **41**, 82 (1969).
- ²⁴J. Kreißl, *Phys. Status Solidi A* **97**, 191 (1986).
- ²⁵H. Zhou, D. M. Hofmann, A. Hofstaetter, and B. K. Meyer, *J. Appl. Phys.* **94**, 1965 (2003).
- ²⁶M. Diaconu, H. Schmidt, A. Pöpl, R. Böttcher, J. Hoentsch, A. Klunker, D. Spemann, H. Hochmuth, M. Lorenz, and M. Grundmann, *Phys. Rev. B* **72**, 085214 (2005).
- ²⁷E. Simánek and K. A. Müller, *J. Phys. Chem. Solids* **31**, 1027 (1970).
- ²⁸W. G. Becker and A. J. Bard, *J. Phys. Chem.* **87**, 4888 (1983).
- ²⁹K. M. Lee, K. P. O'Donnell, and G. D. Watkins, *Solid State Commun.* **41**, 881 (1982).
- ³⁰J. R. James, J. E. Nichols, B. C. Cavennett, J. J. Davies, and D. J. Dunstan, *Solid State Commun.* **17**, 969 (1975).
- ³¹S. C. Erwin, L. Zu, M. I. Haftel, A. L. Efros, T. A. Kennedy, and D. J. Norris, *Nature (London)* **436**, 91 (2005).
- ³²N. Karar, F. Singh, and B. R. Mehta, *J. Appl. Phys.* **95**, 656 (2004).
- ³³M. F. Bulanyi, V. I. Klimenko, A. V. Kovalevko, and B. A. Polezhaev, *Inorg. Mater.* **39**, 436 (2003).

- ³⁴T. Kushida, Y. Tanaka, and Y. Oka, *J. Phys. Soc. Jpn.* **37**, 1341 (1974).
- ³⁵J. Ramírez-Serrano, E. Madrigal, F. Ramos, and U. Caldiño Garcia, *J. Lumin.* **71**, 169 (1997).
- ³⁶W. Q. Peng, S. C. Qu, G. W. Cong, X. Q. Zhang, and Z. G. Wang, *J. Cryst. Growth* **282**, 179 (2005).
- ³⁷Y. Hattori, T. Isobe, H. Takahashi, and S. Itoh, *J. Lumin.* **113**, 69 (2005).
- ³⁸A. Ishizumi, E. Jojima, A. Yamamoto, and Y. Kanemitsu, *J. Phys. Soc. Jpn.* **77**, 053705 (2008).
- ³⁹H.-E. Gumlich, *J. Lumin.* **23**, 73 (1981).
- ⁴⁰W. Busse, H.-E. Gumlich, B. Meissner, and D. Theis, *J. Lumin.* **12/13**, 693 (1976).
- ⁴¹R. S. Meltzer, S. P. Feofilov, B. Tissue, and H. B. Yuan, *Phys. Rev. B* **60**, R14012 (1999).